Constrained Control of Moored Ocean Current Turbines with Cyclic Blade Pitch Variations

Tri D. Ngo[a], Cornel Sultan[1,b], James H. VanZwieten[c], and Nikolaos I. Xiros[d]

[1] Corresponding Author

[a] Tri D. Ngo is with Ho Chi Minh City University of Technology, Ho Chi Minh City, Vietnam; previously with Virginia Tech, Blacksburg, VA 24061 USA (e-mail: ngodinhtri@hcmut.edu.vn or tdn12aoe@vt.edu)

[b] Cornel Sultan is with Virginia Tech, Blacksburg, VA 24061 USA (e-mail: csultan@vt.edu).

[c] James H. VanZwieten is with Florida Atlantic University, Boca Raton, FL 33431 USA. (e-mail: jvanzwi@fau.edu).

[d] Nikolaos I. Xiros is with the University of New Orleans, New Orleans, LA 70148 USA (e-mail: nxiros@uno.edu).

***Abstract*—A new method to control an Ocean Current Turbine (OCT) is examined. The key innovation, inspired by helicopter control, is to use cyclic blade pitch angle variations. Output Variance Constrained (OVC) controllers are designed for OCT flight control and their performance is analyzed.**

***Index Terms*— Hydrokinetic Power, Marine Renewable Energy, Ocean Current Turbines, Numerical Simulation, Output Variance Constrained Control, Flight Control, Ocean Energy Utilization.**

I. Introduction

ESTIMATED U.S. annual electricity production potential from open ocean currents using ocean current turbines (OCTs) is 169 TWh [1]. Time averaged power densities of this resource reach 3.3 kW/m^2, with the main U.S. resource located between South Florida and North Carolina [2]. A cross-section of the ocean current average power density between the U.S. and Bahamas at 27° N (Fig. 1) highlights the importance of OCT location [2]. Ocean current resources targeted off North Carolina, Japan, and South Africa also decay rapidly with depth below the sea surface [3-5]. Therefore, OCTs will ideally operate within the top 50-100 m

of the water column, where the current is strongest. Because of this desired operating location, OCTs will likely be moored to the sea floor. Mooring systems introduce major challenges such as minimizing OCT motions, locating OCTs at the desired depth, controlling their motion to avoid negative interaction with other systems, etc. An approach for experimentally investigating mooring system dynamics associated with OCTs was presented by [3], and several recent studies have been conducted with a focus on increasing the power produced by marine renewable energy devices [6-9] in an attempt to make this form of energy generation more cost competitive.

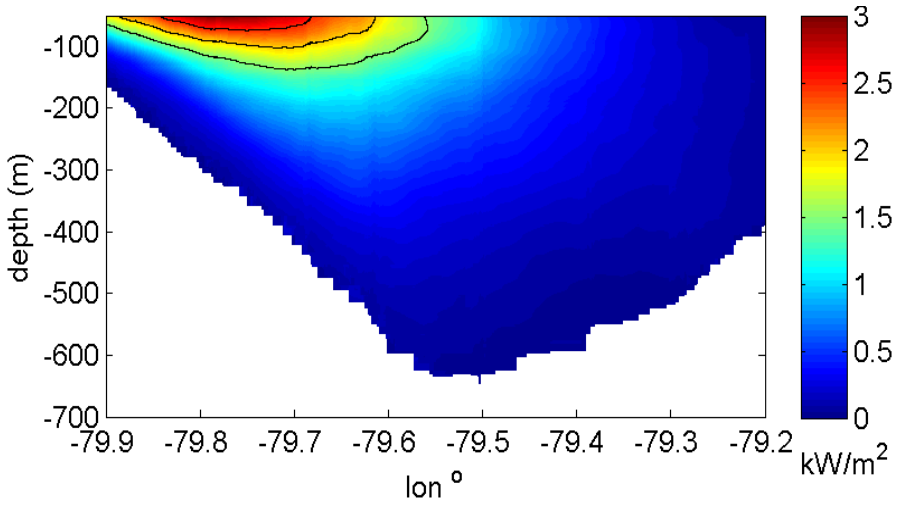

Fig. 1 Average kinetic power density calculated from 35 transects made at 27°N latitude. Contour lines are provided at 1.5, 2.0, 2.5 kW/m^2.

Flight control systems that use wing-like lifting surfaces to control OCT height, pitch and roll with mixed PID/Bang-Bang, LQR/PID/Bang-Bang, and LQG/PID/Bang-Bang approaches were developed and compared via simulations [10]. An open-loop investigation into the development of flight control systems that utilize the rotor blades of co-axial counter-rotating rotors has also been conducted using both numerical and experimental means, demonstrating the capability of moving OCTs approximately perpendicular to the flow [11]. It has also been demonstrated that yaw and roll moments caused by inhomogeneous flow conditions can be balanced by altering the pitch angles of OCT rotor blades [12].

In this article we use a numerical simulation model of a moored OCT, which utilizes a modeling approach based on [13]. This model includes a Blade Element Momentum (BEM) rotor model, as well as the effects

of waves, current shear, and turbulence in hydrodynamic calculations. Details on the updates made to model the 700 kW OCT with a 20 m diameter variable pitch rotor used here are presented in [14]. In [14] an open-loop system analysis is also presented, whereas this article is devoted to feedback control studies.

OVC control has been used in vehicles and structures [15-19], and recently introduced in OCTs [20]. The preliminary analysis in [20] is significantly expanded here by a thorough analysis of OVC control performance, including the effects of constraint limits, process noise, control penalty matrix, and measurements. The key proposed control system technology innovation is to use cyclic blade pitch angle variations in OCT output variance constrained flight control. Note that this is a conceptual study, aimed at illustrating the advantages of OVC control in OCT management. All sensors and actuators are considered ideal, their placement on the OCT is considered to have a negligible influence.

Section II gives a description of the OCT. In Section III the linearization of the nonlinear OCT simulation model around a nominal operating condition is presented, as well as a stability analysis. In Section IV OVC control is revisited. Section V presents the application of OVC control to OCT and comprehensive evaluations. Conclusions are given in Section VI.

II. OCT System Description

A. Nonlinear Ocean Current Turbine Model

The 24.8 m long horizontal axis nearly neutrally buoyant OCT, with a 20 m diameter rotor and two 15.6 m long buoyancy compensation modules, designed by the Southeast National Marine Renewable Energy Center [14,21] to produce up to 700 kW is used here (Fig. 2). Rotor airfoils range from nearly cylindrical at the hub to a FX-83W airfoil with a thickness ratio of 21% at 20% of the rotor radius and FX-83W with a thickness ratio of 10.8% at the blade tip. The airfoils at these locations have maximum two-dimensional (2D) lift coefficients of 1.4 and 1.62 at angles of attack of 16° and 17° respectively (calculated using X-Foil). These coefficients are modified to account for 3D effects using the Du-Selig and Eggers corrections, resulting in maximum lift coefficients of 2.02 and 1.54 at angles of attack of 32° and 16.5° (calculated using

AirfoilPrep). This OCT is attached, via a cable, to a flounder plate connected to a mooring line that runs from a surface buoy to the sea floor [14,21].

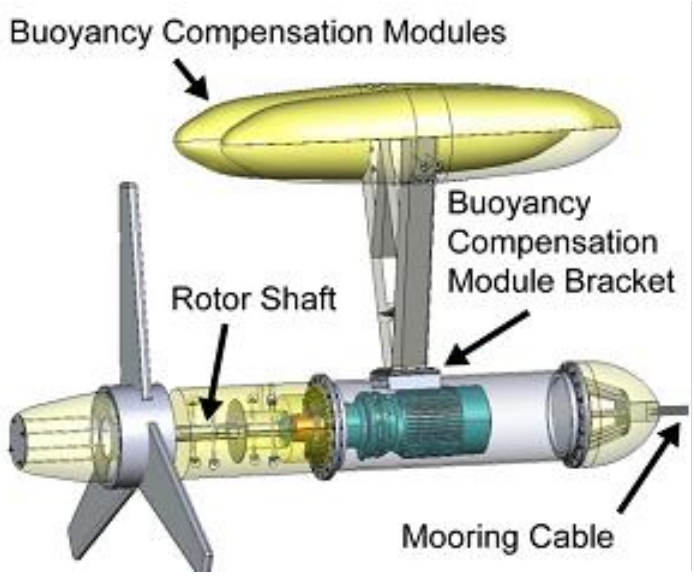

Fig. 2 Artist rendering of the OCT with major components listed [13].

The rigid body dynamics of this turbine, including the effects of the cable, are considered in the nonlinear simulation. Modeling techniques used to represent rotor and cable forces are individually validated for other applications. The rotor modeling process [13] is theoretically similar to those utilized to create time domain simulations of wind turbines, such as the extensively validated and certified National Renewable Energy Laboratory's AeroDyn aerodynamics module that is used for turbine design and analysis [22]. The rotor and blades are modeled as being rigid, and hydrodynamic forces are calculated using the Blade Element Momentum (BEM) approach [23]. This calculates the forces on individual blade sections using a blade element (BE) approach that accounts for the relative water velocity at each blade section. Calculated forces are then used to update the inflow velocity using a momentum (M) approach. A grid fixed to the swept area of the rotor is used to calculate these impeded flow values using a dynamic wake approach. Impeded flow values at each blade element are calculated for each time step from values on this grid at the adjacent radial grid points. The motion of rotor elements, freestream flow velocities, and calculated impeded flow values are then used to calculate the relative flow velocity and angle of attack of each blade element. Forces on blade elements are integrated along the blade length to obtain rotor hydrodynamic forces and moments. The

hydrodynamic models used to compute forces on non-rotor turbine components, as well as the cable model, are described in [13]. Hydrodynamic forces that act on the main body, two buoyancy compensation modules, and cable elements are calculated each time step. These forces, along with gravity, buoyancy, and elastic cable forces are used to compute OCT motion. The OCT's degrees of freedom (DOF) values are calculated as described in [14].

A finite-element lumped mass cable modeling technique is used for the 607 m cable that attaches the ocean current turbine to the flounder plate, adding 3 DOFs per each cable node that is not attached to the turbine or flounder plate. This model was developed and validated for tethered Remotely Operated Vehicles [24] and has also been applied to towed sensor systems [25]. In the model each numerically modeled cable element is assumed to be linear and elastic, with the mass of the cable lumped at the nodes which connect these linear elements. Velocity and position for the end nodes are defined by the position, velocity, orientation, and angular velocity of the OCT at one end and the position of the flounder plate at the other. All intermediate nodes are initially allowed to settle to their equilibrium locations, based on the initial states of the OCT and flounder plate, before each numerical simulation is run. Linear accelerations for each intermediate node are found using the sum of forces calculated on neighboring cable elements (F) and the mass of each element (m) according to $a_{node} = F/m$. These accelerations are numerically integrated to calculate the velocities of the nodes and again to calculate node positions. Forces from gravity, buoyancy, hydrodynamic drag, and internal strain (in tension, not compression) are included in this model. The cable characteristics are set to match that of a 0.085 m diameter wire rope, with a total mass of 19,250 kg and a total buoyancy force of 32 kN. Sensitivity analyses showed that increasing the number of cable elements beyond 5-8 only minimally impacts the OCT performance [26]. Thus, 5 cable elements are used for nonlinear simulations.

B. Individual Blade Pitch Control (IBC)

For OCT control IBC is used. Standard IBC is realized using collective control, which simultaneously modifies all blade pitch angles by the same value, and cyclic controls which ensure that each blade pitch

angle varies harmonically with the azimuth (the angle made by the blade with a fixed direction in the rotor plane). In analogy with helicopter control [27], cyclic blade pitch angles are controlled using a swashplate (Fig. 3). IBC oscillates each blade's root pitch angle about the collective pitch angle, γ_{eq}, corresponding to maximum power production. For three synchronously rotating blades the blade pitch root angles are:

$$\begin{bmatrix}\gamma_1\\ \gamma_2\\ \gamma_3\end{bmatrix}=\begin{bmatrix}1\\ 1\\ 1\end{bmatrix}\gamma_{eq}+\begin{bmatrix}\sin\alpha & \cos\alpha\\ \sin(\alpha+2\pi/3) & \cos(\alpha+2\pi/3)\\ \sin(\alpha+4\pi/3) & \cos(\alpha+4\pi/3)\end{bmatrix}\begin{bmatrix}\gamma_a\\ \gamma_b\end{bmatrix}, \tag{1}$$

where γ_a and γ_b are cyclic control inputs and α is the azimuth angle of the first blade. The electromechanical rotor torque is the third control input of the OCT.

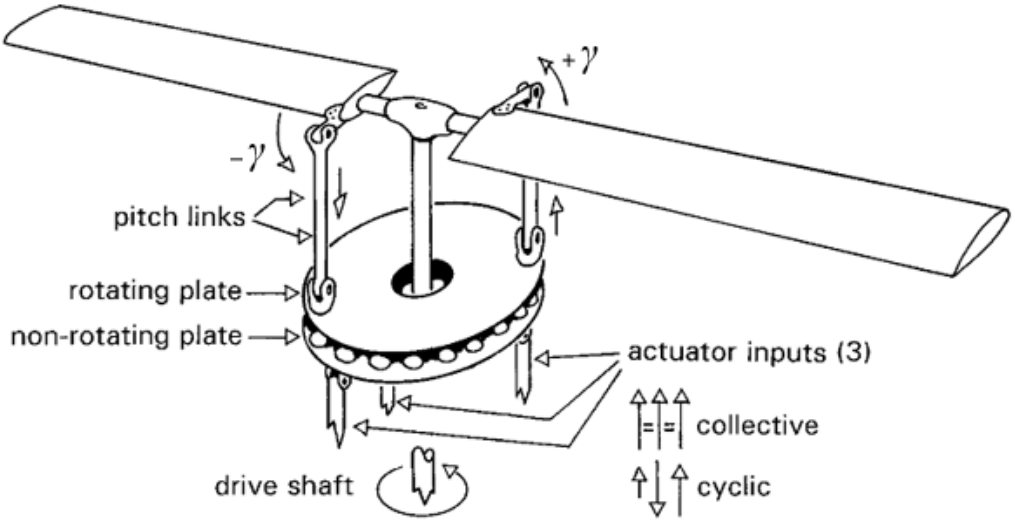

Fig. 3 Rotor blade control through a swashplate [28].

III. Linearized Model Analysis

A. Linearized Model

The states used in the linearized OCT model are deviations from the nominal values of translational and angular velocities of the OCT body in the OCT body fixed reference frame, u, v, w, p, q, r, rotor angular speed with respect to the OCT body, ω, Cartesian coordinates of the location where the rotor axis coincides with the central plane of the rotor hub in the inertial frame, x, y, z, and Euler angles describing the orientation of the OCT body fixed reference frame with respect to the inertial reference frame, ϕ, θ, ψ. The inertial

reference frame is a right-handed system defined such that its *z*-axis (vertical) points downwards, its *x*-axis is aligned with the mean flow direction and its *y*-axis (lateral) results from the right handed condition. The origin of the inertial frame is set to the location of the flounder plate. During nominal operation the *x*-axis points towards the right in Fig. 2. The body fixed frame is a right handed system attached to the OCT, defined such that its z_b-axis points from the top to bottom of the OCT and its x_b-axis is aligned with the rotor axis of rotation. The y_b-axis results from the right handed condition. Fig. 4 shows the inertial and turbine reference axes along with key dimensions. The OCT state and control vectors used in the linearized model are, therefore,

$$\delta x_p = [\delta u \quad \delta v \quad \delta w \quad \delta p \quad \delta \omega \quad \delta q \quad \delta r \quad \delta x \quad \delta y \quad \delta z \quad \delta \phi \quad \delta \theta \quad \delta \psi]^T \text{ and } \delta u_p = [\delta \gamma_a \quad \delta \gamma_b \quad \delta \tau_{em}]^T,$$

and the corresponding linearized model can be formally written as $\delta \dot{x}_p = A_p \delta x_p + B_p \delta u_p$ where δ denotes the difference between the state or control vectors and the equilibrium values about which the system is linearized. For notational simplicity, δ has been omitted from the linearized model in subsequent sections.

To determine matrices A_p and B_p the nonlinear OCT model is linearized around a nominal condition for maximum power produced in steady axial flow. This condition is characterized by averaged flow velocity of 1.6 m/s. The resulting equilibrium control values are $u_{EQ} = [0° \quad 0° \quad -246.5\, kNm]^T$ and the corresponding equilibrium states are $x_{EQ} = [0 \quad 0 \quad 0 \quad 0 \quad 14.17\, RPM \quad 0 \quad 0 \quad -623.1m \quad 0.3m \quad 10.5m \quad 0.8° \quad -2.7° \quad 0.0°]^T$. It is noted that in this model both the hydrodynamic and electromechanical torques are defined as positive when they produce a positive (with respect to the x_b-axis) moment on rotating components. Therefore, electromechanical torque values are negative when shaft power is converted into electricity. Note that the values of the states and controls corresponding to the nominal condition are referred to as nominal or equilibrium values.

For linearization, all intermediate cable nodes are assumed in equilibrium. Quasi-static cable force dependencies on OCT position and attitude are determined by re-calculating equilibrium cable node states

and the resulting forces on the OCT during linearization each time the OCT position or attitude states are varied [28]. Dependencies of cable forces on the OCT velocity states are accounted for during linearization by allowing velocity perturbations to alter cable node position and velocity equilibrium states. This allows the effects of changes in all OCT states to be incorporated into the linear model, without directly accounting for the individual cable node states. Utilizing this approach, the matrices of the linearized model corresponding to the x_{EQ} and u_{EQ} values presented in the previous paragraph are found. These matrices are presented in the following tables:

Matrix A_p

-3.13E-01	-7.90E-02	-6.00E-03	-2.18E-01	-2.21E-01	-3.66E-01	1.83E-01	-5.80E-02	8.51E-05	-3.00E-03	-1.03E-02	-1.17E+00	-2.95E-03
3.11E-03	-1.56E-01	6.02E-01	1.75E-01	-6.70E-04	1.58E+00	1.90E+00	-3.90E-05	1.06E-03	1.17E-05	1.15E+00	-7.13E-02	9.40E-01
-6.73E-02	-4.60E-01	-1.94E-01	-5.65E-02	-5.75E-02	-8.34E-01	1.17E+00	-1.78E-02	1.50E-05	-4.60E-04	-2.30E-03	-3.77E+00	-4.99E-02
9.50E-05	-4.73E-02	-8.41E-03	-6.59E-01	-6.97E-05	-3.02E-02	-3.79E-01	0.00E+00	2.30E-04	2.54E-06	-1.46E+00	-5.17E-03	2.22E-01
5.46E-01	-7.25E-06	-8.09E-05	-2.57E-01	-2.56E-01	-2.66E-02	-3.85E-03	1.79E-11	0.00E+00	0.00E+00	-4.71E-01	2.80E-02	-2.62E-04
-1.17E-02	-4.35E-02	-4.61E-03	-8.80E-03	-8.96E-03	-2.42E-01	1.04E-01	-2.58E-03	-1.10E-06	6.89E-05	-5.88E-05	-6.32E-01	-7.56E-03
-4.19E-04	1.22E-02	-6.35E-02	2.13E-02	1.58E-04	-1.58E-01	-3.07E-01	1.33E-05	-3.63E-04	-4.00E-06	2.38E-01	1.21E-02	-2.52E-01
9.99E-01	-1.05E-03	-4.62E-02	0.00E+00	0.00E+00	0.00E+00	0.00E+00	0.00E+00	0.00E+00	0.00E+00	0.00E+00	0.00E+00	0.00E+00
4.30E-04	1.00E+00	-1.35E-02	0.00E+00	0.00E+00	0.00E+00	0.00E+00	0.00E+00	0.00E+00	0.00E+00	0.00E+00	0.00E+00	0.00E+00
4.62E-02	1.34E-02	9.99E-01	0.00E+00	0.00E+00	0.00E+00	0.00E+00	0.00E+00	0.00E+00	0.00E+00	0.00E+00	0.00E+00	0.00E+00
0.00E+00	0.00E+00	0.00E+00	1.00E+00	0.00E+00	-6.22E-04	-4.63E-02	0.00E+00	0.00E+00	0.00E+00	0.00E+00	0.00E+00	0.00E+00
0.00E+00	0.00E+00	0.00E+00	0.00E+00	0.00E+00	1.00E+00	-1.34E-02	0.00E+00	0.00E+00	0.00E+00	0.00E+00	0.00E+00	0.00E+00
0.00E+00	0.00E+00	0.00E+00	0.00E+00	0.00E+00	1.34E-02	1.00E+00	0.00E+00	0.00E+00	0.00E+00	0.00E+00	0.00E+00	0.00E+00

Matrix B_p

-2.94E-01	-3.57E-02	-2.38E-15
-1.38E-01	1.49E+00	7.77E-08
-1.05E+00	-1.10E-01	-9.71E-15
1.41E-03	6.47E-02	-7.83E-08
-2.29E-02	-2.61E-03	1.85E-06
-1.63E-01	-1.12E-02	-9.62E-16
1.51E-02	-2.51E-01	1.01E-08
0.00E+00	0.00E+00	0.00E+00
0.00E+00	0.00E+00	0.00E+00
0.00E+00	0.00E+00	0.00E+00
0.00E+00	0.00E+00	0.00E+00
0.00E+00	0.00E+00	0.00E+00
0.00E+00	0.00E+00	0.00E+00

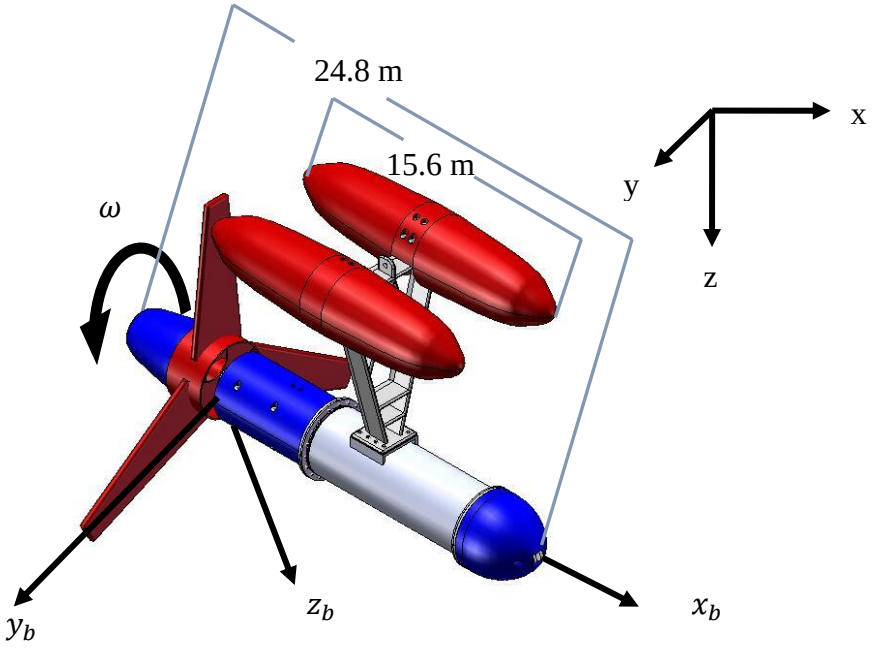

Fig. 4 OCT key dimensions and reference frames

For similarity and non-dimensionalization purposes, OCT models are normalized by dividing angular velocities by the nominal rotor angular rate (14.17 RPM), lengths by the rotor blade length (10 m), translational velocities by the tip blade velocity (14.84 m/s), and linear accelerations by the tip blade acceleration (22.01 m/s^2). The turbine mass is 4.98x10^5 kg, rotor mass is 6.16x10^4 kg, and its longitudinal moment of inertia is 5.39x10^5 kg·m^2.

B. Stability Analysis

The eigenvalues of the linearized model's state matrix are:

$$\begin{aligned} &-0.2737 \pm 1.1842i, && -0.1242 \pm 0.1751i, \\ &-0.2372 \pm 0.9944i, && -0.0012 \pm 0.0016i, \\ &-0.2344 \pm 0.3942i, && -0.0656. \\ &-0.1599 \pm 0.4446i, \end{aligned} \tag{2}$$

Eigenvector analysis showed that the dominant motions corresponding to the lightly damped eigenvalues, -0.0656, -0.0012 ± 0.0016*i*, affect the OCT coordinates (see Table 1 which provides eigenvectors corresponding to -0.0656 and -0.0012 + 0.0016 *i*, with the phase given in degrees). Thus, perturbations in

the OCT position will be eliminated in a very long time, i.e. the OCT will return to the unperturbed nominal operating condition very slowly. However, OCTs must restore their position to the unperturbed nominal operating condition in relatively short time scales to avoid interference with shipping traffic or neighboring OCTs when deployed in arrays. Also, for optimal energy harvesting OCTs must operate close to the water surface (Fig. 1). Therefore, OCT feedback control is needed in order to contain the state vector within a sufficiently small neighborhood of the nominal condition as well as guarantee speedy disturbance rejection and error mitigation.

TABLE I: Eigenvector Analysis of the Linear OCT Model

Eigenmodes		**-0.0656**		**-0.0012 + 0.0016i**	
States		**Magnitude**	**Phase**	**Magnitude**	**Phase**
1	*u*	2.14E-02	180	1.31E-05	-41
2	*v*	2.63E-03	180	1.64E-03	55
3	*w*	8.99E-04	180	1.12E-03	133
4	*p*	9.47E-06	180	3.32E-07	-159
5	ω	6.18E-02	180	1.59E-04	141
6	*q*	8.63E-06	180	6.10E-07	126
7	*r*	1.34E-05	180	2.99E-06	-134
8	*x*	3.26E-01	0	3.28E-02	78
9	*y*	4.00E-02	0	8.21E-01	-180
10	*z*	2.94E-02	0	5.65E-01	-102
11	ϕ	1.35E-04	0	1.08E-04	-49
12	θ	1.29E-04	0	3.10E-04	-112
13	ψ	2.06E-04	0	1.50E-03	-8

To verify the linearization process, we performed extensive comparisons between OCT nonlinear and linear model responses. For example, Figs. 5-7 show responses to torque and cyclic blade pitch angle control input steps. Note that in these Figures deviations from nominal values are depicted (e.g., τ_{em} is the deviation of the electromechanical torque from its nominal value of $-246.5\ kNm$, etc.). The position states predicted by the linear and nonlinear models are in good agreement, with the greatest error occurring in the cross-stream direction, δY, where the linear model calculated a displacement of 26.6 m compared to 22.7 m for the nonlinear model 30 minutes after a step increase of $2°$ was made to γ_b. Small disagreement is observed in the rotor speed response to the cyclic blade pitch angle control input, with the linear model predicting a

rotor rotational velocity that was greater than the nonlinear model by 0.23 RPM for $\gamma_a = 2°$ and 0.59 RPM for $\gamma_b = 2°$. This discrepancy is due to the fact that the linear model does not capture the relationship between flow misalignment and hydrodynamic rotor torque. This relationship is not captured because the linearization was carried out about equilibrium pitch/yaw angles where the rotor is nearly aligned with the flow, which is at the peak of a symmetric relationship between pitch/yaw and hydrodynamic rotor torque.

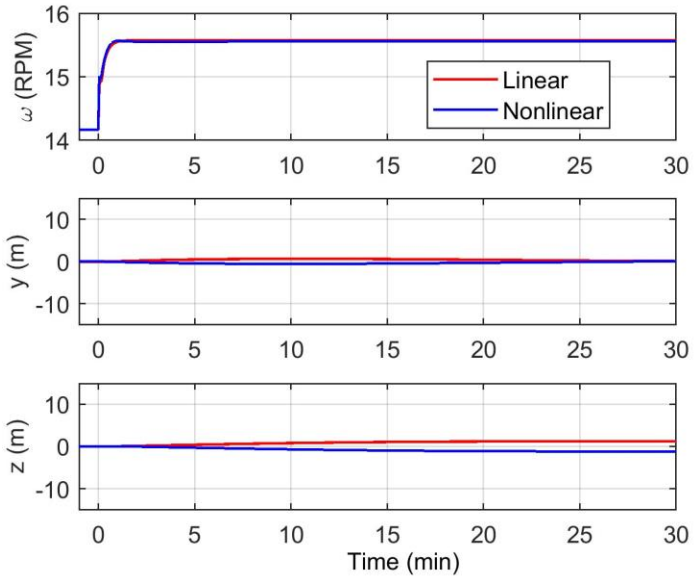

Fig. 5 OCT response to 20kN step torque input increase in the direction of rotor rotation

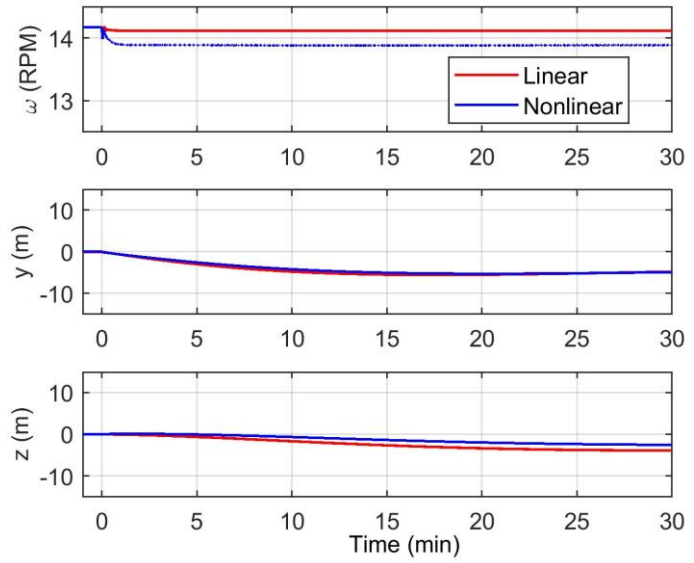

Fig. 6 OCT response to 2° step increase in the cyclic blade pitch angle control input γ_a

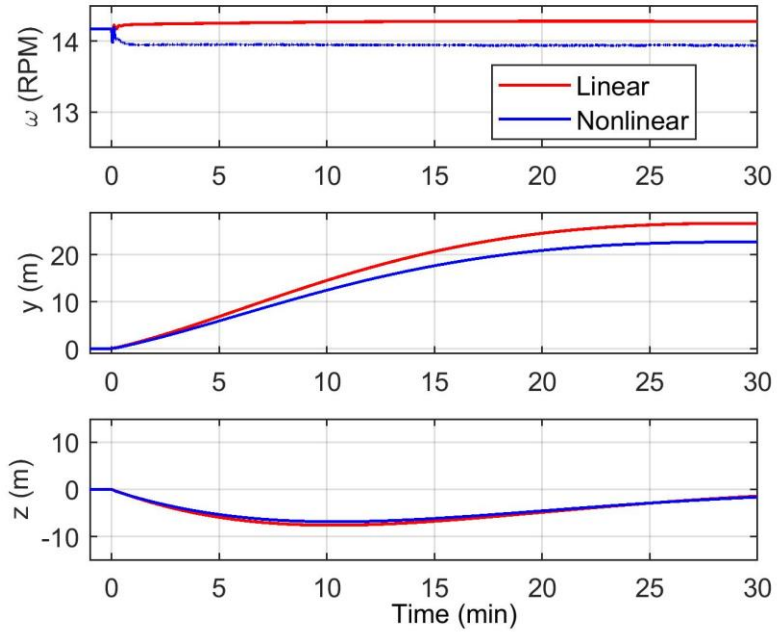

Fig. 7 OCT response to 2° step increase in the cyclic blade pitch angle control input γ_b

IV. Output Variance Constrained Control

One of the typical objectives in control design is minimization of control energy. In addition, realistic control design must take into account constraints (e.g., on the controls, outputs, or other variables). In this article, we employ a modern control technique which minimizes control energy and guarantees that output variations remain confined to a neighborhood of zero by requiring that the output variances are upper bounded. These objectives are consistent with the overall goal of maximizing the energy generated by the OCT because the energy required to operate the control system (i.e. the control energy) will be on the expense of the energy harvested. Also, in simple terms, the variance measures how far some random numbers are spread out from their average value. Therefore, a small variance indicates less variability around the mean value of the variable, which is a desired feature. By requiring that the control system ensures satisfaction of stringent upper bound constraints on output variances, these will have small values, which is consistent both with the linearization assumption and with the overall goal of the control system to regulate around a nominal

operation condition and keep variations small. This technique, called output variance constrained (OVC) control, is described next.

Consider the generic (linear time invariant) LTI system

$$\dot{x}_p = A_p x_p + B_p u_p + D_p w_p,\ y_p = C_p x_p,\ z_p = M_p x_p + v_p \tag{3}$$

and a strictly proper output feedback controller

$$\dot{x}_c = A_c x_c + F z_p,\ u_p = G x_c \tag{4}$$

where x_p, x_c, y_p, z_p,, u_p are plant state, controller state, output, measurement, control vectors, while w_p, v_p are zero-mean uncorrelated Gaussian white noises with intensities W_p and V_p, respectively. The closed-loop system, obtained by combining the open loop system (3) with the controller in (4), is

$$\dot{x}_{cl} = A_{cl} x_{cl} + D_{cl} w_{cl}, y_{cl} = C_{cl} x_{cl} \tag{5}$$

Here $x_{cl} = [x_p^T \quad x_c^T]^T$, $y_{cl} = [y_p^T \quad u_p^T]^T$, $w_{cl} = [w_p^T \quad v_p^T]^T$, and the closed loop matrices are

$$A_{cl} = \begin{bmatrix} A_p & B_p G \\ F M_p & A_c \end{bmatrix},\ D_{cl} = \begin{bmatrix} D_p & 0 \\ 0 & F \end{bmatrix},\ C_{cl} = \begin{bmatrix} C_y \\ C_u \end{bmatrix},\ C_y = \begin{bmatrix} C_p & 0 \end{bmatrix},\ C_u = \begin{bmatrix} 0 & G \end{bmatrix}. \tag{6}$$

Physically, the closed loop system is obtained by feeding the sensor measurements (i.e. the elements of z_p) into the control computation block which generates the control input vector, u_p, applied to the system.

The first goal of any feedback controller is to ensure that A_{cl} is exponentially stable (i.e. it has eigenvalues with strictly negative real parts). Then the closed-loop covariance, X_{cl}, satisfies the following Lyapunov equation, $A_{cl} X_{cl} + X_{cl} A_{cl}^T + D_{cl} W D_{cl}^T = 0$, where $W = diag\begin{bmatrix} W_p & V_p \end{bmatrix}$. The control energy is defined as $J = E_\infty u_p^T R u_p$ where $E_\infty = \lim_{t\to\infty} E$ with E the expectation operator and can be easily computed as $J = tr\left(R C_u X_{cl} C_u^T\right)$ where "tr" is the trace operator. Also the output variances, defined as $Y_i = E_\infty y_{pi}^2$, $i = 1, \ldots, n_y$, are the diagonal elements of the matrix $Y = C_y X_{cl} C_y^T$.

The OVC control design problem consists in finding a feedback dynamic controller defined by Eq. (4) (i.e.

finding matrices A_c, F, G) which minimizes the control energy subject to output variance constraints [29-30]. Mathematically the problem is formulated as

$$\min_{A_c,F,G} E_\infty u_p^T R u_p \text{ subject to } E_\infty y_{pi}{}^2 \le \bar{Y}_i, i = 1,...n_y \quad (7)$$

where $R>0$ is the control penalty matrix and $\bar{Y}_i$ are user prescribed upper bounds on the output variances.

The control penalty matrix enables different weightings on individual controls. For example, if R is diagonal, like in the examples included in this article, the maximum diagonal element of R will enforce a smaller variation of the corresponding control input. The utility of R will be clear in the examples section where it will enable studies on blade stall likelihood.

OVC control problem solution reduces to linear quadratic Gaussian (LQG) control design by choosing the output penalty $Q \ge 0$ in LQG control, function of the output variances upper bounds in (7), $\bar{Y}_i$. An algorithm for Q selection is presented in Refs. [29,30] and used here. Then the OVC control matrices are $A_c = A_p + B_p G - F M_p$, $G = -R^{-1} B_p^T K$, $F = \tilde{X} M_p^T V_p^{-1}$ where K and $\tilde{X}$ are obtained from two Riccati equations (see [29] for detailed proofs):

$$A_p^T K + K A_p - K B_p R^{-1} B_p^T K + C_p^T Q C_p = 0, A_p \tilde{X} + \tilde{X} A_p^T - \tilde{X} M_p^T V_p^{-1} M_p \tilde{X} + D_p W_p D_p^T = 0. \quad (8)$$

A major advantage for practical implementation and real-time operation of this dynamic feedback controller is that all controller parameters (i.e. matrices A_c, B_c, G) are computed off-line. Therefore, real-time control using the controller presented in this work is feasible. Note also that a Kalman filter, which enables optimal estimation of the states, is an intrinsic part of the controller used here. Specifically, x_c is the vector of state estimates obtained using the sensor measurements (i.e. the elements of z_p). The second Riccati equation in Eq. (8) provides $\tilde{X}$ which is used to compute the Kalman filter gain F as discussed before, for use in Eq. (4).

The OVC control problem does not have solutions if the limits in (7), $\bar{Y}_i$, are too small [19]. The minimum limits that are theoretically achievable are computed using [30]:

$$\bar{Y}_{i_{\min}} = [C_p \tilde{\bar{X}} C_p^T]_{ii}, \quad i = 1,...,n_y \tag{9}$$

Therefore, before implementation of the OVC algorithm these bounds should be computed and the upper bounds on the output variances $\bar{Y}_i$ must be selected such that $\bar{Y}_i \geq \bar{Y}_{i_{\min}}, i = 1,...,n_y$.

Note that the OCT return speed to the nominal position cannot be directly specified in OVC control however if the upper bounds $\bar{Y}_i$ in (7) are small, the OCT return speed will be small.

V. Application of OVC control to OCT

In OCT control design, measurements are deviations from nominal values of translational and angular velocities, Euler angles, OCT Cartesian coordinates, and rotor angular speed. Controls, or inputs, are deviations from the nominal values of the electromechanical torque and cyclic blade pitch angle inputs. Outputs are deviations from the nominal values of the rotor angular speed and of the lateral and vertical inertial OCT coordinates. These coordinates were selected as outputs because they are critical for safe and optimal OCT operation (Fig. 1) and are affected by lightly damped eigenvalues (Table I). Zero-mean uncorrelated Gaussian white noises, w_p and v_p, are used in (3), with $D_p = I$, where I is the identity matrix, and matrices A_p, B_p derived as described in section III.A, with standard linear controllability tests showed that the system is controllable. Note also that the normalized OCT linear system is used for control design.

A. Influence of the OVC Limits on Control Energy

Using $\bar{Y}_i = a \times \bar{Y}_{i_{\min}}$ in (7) with $a > 1$ enables a parametric study on the influence of the OVC limits on control performance. OVC control design was performed for various values of the scaling factor a. For $W = 2\text{x}10^{-6} I$ the results are shown in Fig. 8. When a approaches 1 the control energy increases rapidly because the theoretical limits (9) are approached. Thus, a trade-off must be made between the OVC limits to be satisfied and the control energy necessary to do so. For further studies, $a = 5$ was selected. Note that the data reported next refers to the linear system.

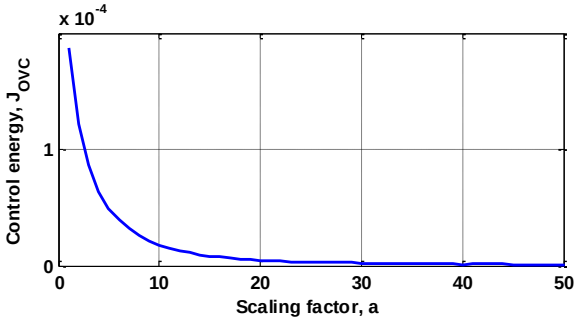

Fig. 8. Control energy variation with the scaling factor a

B. Influence of the Process Noise Intensity on Blade Pitch

Satisfaction of constraints in (7) under high process noise intensity values may require large blade pitch angles, leading to blade stall. Here we assume that if blade pitch angles vary between ±10°, stall is avoided. This assumption was selected based on the hydrofoils having a stall point near 17° and nominal angles of attack near 3° for most radial locations, thus a 14° separation.

Fig. 9 presents results of a study on process noise intensity effects on blade pitch angles. OVC controllers were designed for $a = 5$, $R = I$, and parameterized normalized process noise intensity $W_p = a_w I$, with a_w a scalar. Fig. 9 shows that the minimum, $\gamma_{\min}$, and maximum, $\gamma_{\max}$, blade pitch angles are between ±10° if W_p $<1.44\text{x}10^{-6} I$ and that $\gamma_{\min}$ and $\gamma_{\max}$ decrease, respectively increase, rapidly with a_w. Since process noise intensity is a measure of modeling errors, these results reveal the need for an accurate OCT model. Also, maximum deviations of the closed loop OCT coordinates of interest and rotor angular speed are significantly reduced with respect to the open loop ones. Note that the normalized noise intensity is small. However, normalization involves division of physical quantities by large numbers (see the discussion on normalization in III. *A*.). Thus, noise intensities in the physical space are larger and have realistic ranges.

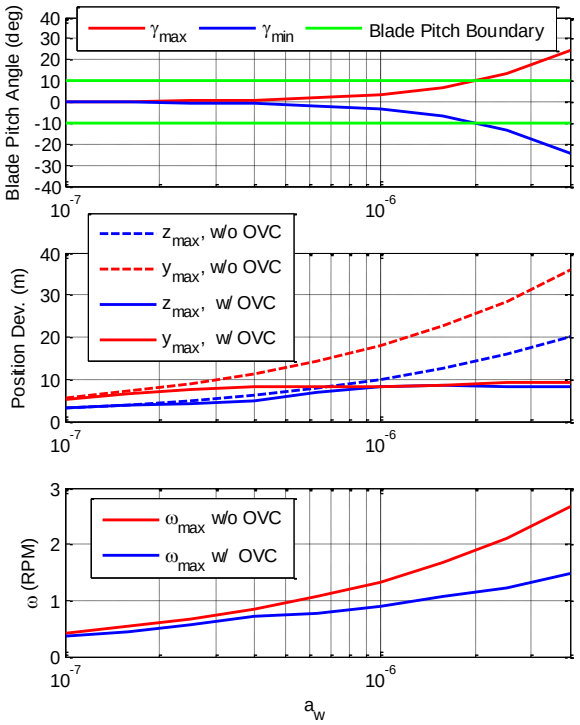

Fig. 9 Minimum and maximum blade pitch angles, maximum position and rotor angular speed deviation variations with process noise intensity (w/o OVC means without OVC control and w/ OVC means with OVC control).

C. Influence of the Control Penalty Matrix on Blade Pitch

For a given control penalty matrix, R, OVC control design, if successful, delivers an output penalty matrix Q. However, R must be defined before OVC control design is performed. To evaluate the influence of R on OVC control we performed a parametric study as follows. Define R as $R = \mathrm{Diag}[\lambda \quad \lambda \quad 1]$. Because the first two components of the control vector are the cyclic blade pitch angle control inputs, this structure of R ensures that λ is directly related to these controls. Thus, λ has direct influence on blade pitch angles, so by choosing this parameter blade stall can be avoided.

OVC controllers were designed for $a = 5$, $W = 1.4\text{x}10^{-6}I$, and various λ values. The minimum and maximum blade pitch angle variations with λ (Fig. 10) show that for $\lambda > 0.25$ the ±10° limits on the blade pitch angles are satisfied. This behavior is expected because larger λ results in smaller blade pitch angle control inputs. Note that the minimum and maximum blade pitch angle variations with λ are less pronounced compared to the variations with respect to a_w (see Figs. 8 and 9). This suggests that modeling errors, quantified by process noise intensity, are more influential on blade stall than the control penalty matrix in OVC control design.

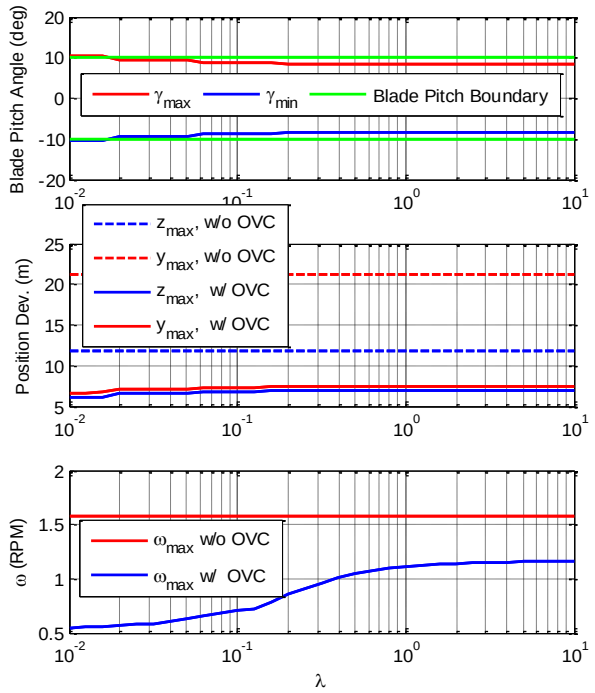

Fig. 10 Variation of the minimum and maximum blade pitch angles with λ

D. System Response to External Disturbances

To further evaluate closed-loop system performance, various external disturbances were applied. Fig. 11 shows open and closed loop system responses to lateral (y) and vertical (z) disturbances of 5 m. The OVC controller, designed for a = 5, λ = 0.25, $W = 1.4\text{x}10^{-6}I$, restores the OCT to its original position in about 10 minutes, while in open loop configuration it takes 1.67 hours for the disturbed position to converge within about 1m of the original, unperturbed position. The closed-loop rotor angular speed variation is very small, with a maximum of about 0.55 RPM. The closed-loop control variations are also small: the maximum for γ_a is less than 4°, for γ_b about 1°, while the maximum torque deviation is 11%. Fig. 12 depicts open- and closed-loop system responses to white noise disturbances of the same intensities as the ones used in OVC control design. Improvement when feedback control is used is evident.

Fig. 13, the counterpart of Fig. 12 obtained for an OVC controller designed for a = 3, shows that blade pitch angle control input variations are larger than for a = 5. This reveals that more stringent OVC constraints increase stall danger.

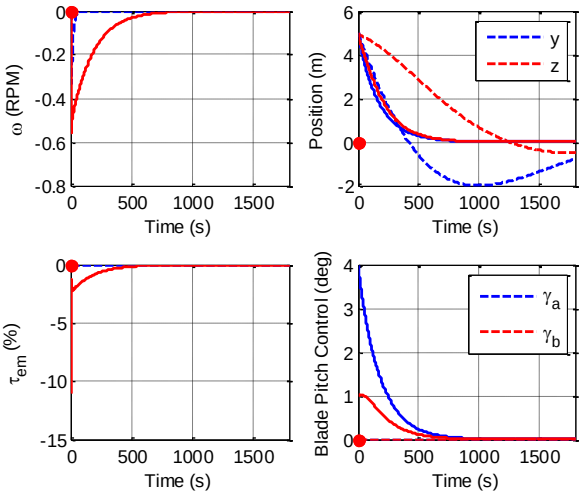

Fig. 11 System responses to initial condition perturbation (solid lines: closed loop, dash lines: open loop, red dots: nominal) for $a = 5$

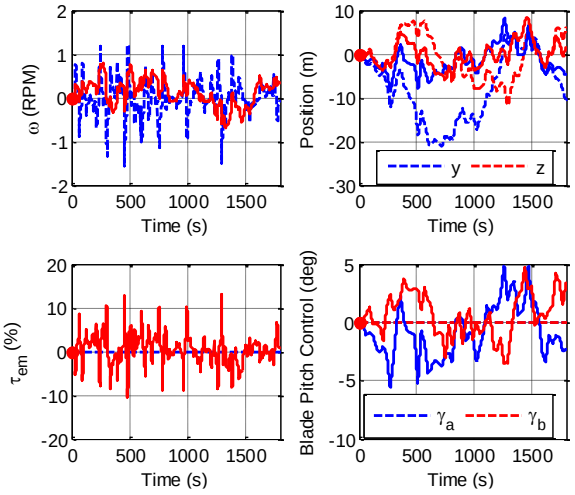

Fig. 12 System responses to white noise disturbances (solid lines: closed loop, dash lines: open loop, red dots: nominal) for $a = 5$

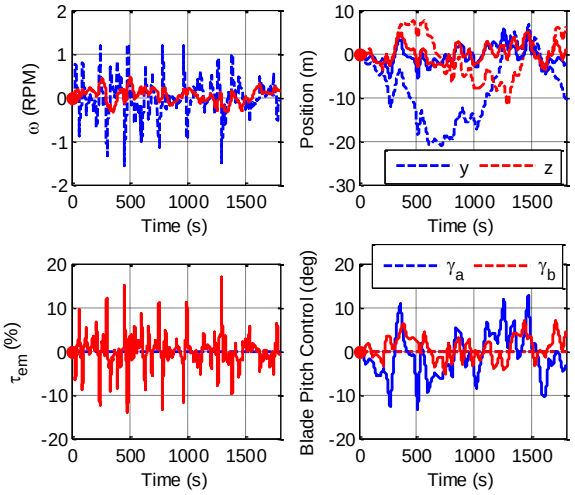

Fig. 13 System responses to white noise disturbances (solid lines: closed loop, dash lines: open loop, red dots: nominal condition) for $a = 3$

Figs. 14-15 show a comparison between linear and nonlinear closed-loop system responses when the same OVC controller is used. The OCT is disturbed by 5 m laterally and 2 m vertically from the nominal operating condition. Nonlinear simulations show that the controller restores the OCT to its initial position within about 600 seconds, while linear simulations show that the controller restores the OCT to its initial position in about 500 seconds. This discrepancy can be explained by the fact that the mooring cable dynamics was neglected in the linear model. The cable is very flexible and has a destabilizing effect which is accounted for in the nonlinear OCT model. Fig. 15 shows that nonlinear and linear closed loop system responses are close.

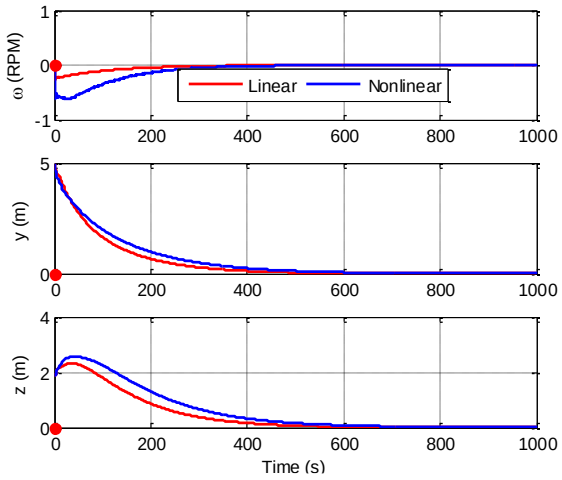

Fig. 14 Nonlinear and linear closed loop system output responses

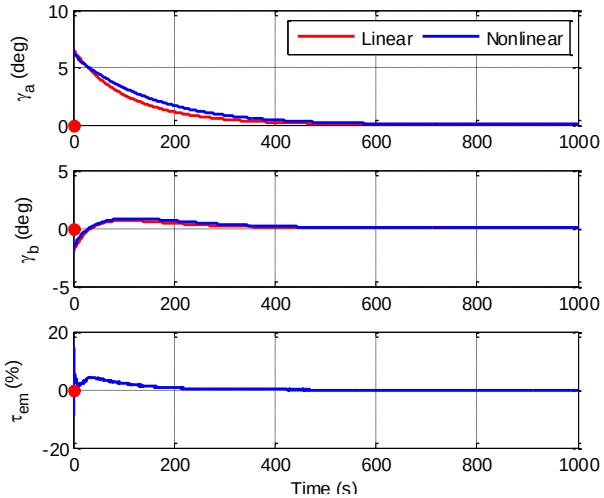

Fig. 15 Nonlinear and linear closed loop system control responses

E. Robustness Analysis

For an evaluation of OVC control robustness, the controller designed for the nominal condition and for a = 5, λ = 0.25, W = 1.4x10^{-6}I, was implemented on perturbed plants. These were generated using $A_p^{perturbed} = M_A A_p$, $B_p^{perturbed} = M_B B_p$, where M_A and M_B are matrices of pseudo-random values drawn from the standard uniform distribution in the interval (-1.05; 1.05). In addition, elements in A_p and B_p that are known from the mathematical construction of the linear model to be unaffected by uncertainties were not modified (e.g., certain 0 and 1 values). Fig. 16 shows the standard deviations of the perturbations (abbreviated as STDV) from equilibrium values of the rotor angular speed, lateral and vertical OCT coordinates in response to white noise disturbances of the same intensities as the ones used in OVC control system design for 200 test cases. It can be ascertained that the nominal design is sufficiently robust (similar results were obtained for pseudo-random values in M_A and M_B drawn from intervals as large as (-1.1; 1.1)). Moreover, since the perturbations considered are not tied to specific OCT parameters (e.g. mass, rotor diameter) or nominal operating condition (e.g. axial flow velocity, nominal angular speed), the results suggest that the controller is robust even with respect to more specific perturbations.

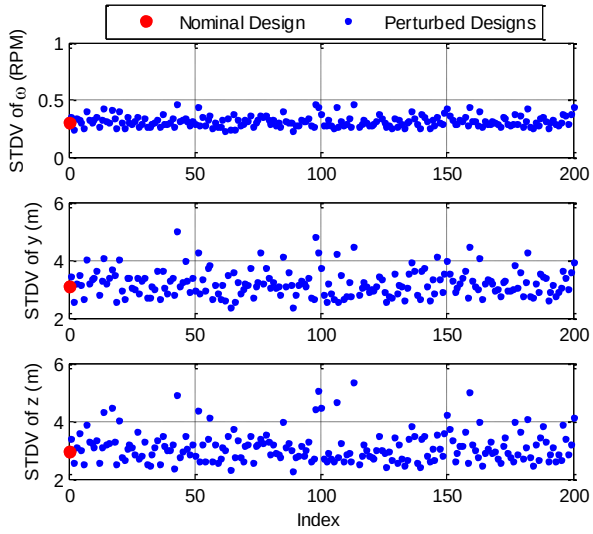

Fig. 16 Robustness results for the closed loop system.

370 *F. OVC Control without Position Sensors*

371 In the previous analyses the ideal situation was considered, when all OCT states used in the linear model
372 are measured. In reality, OCT Cartesian coordinates are difficult to measure due to the lack of GPS signal in
373 deep water. An inertial navigation system (INS) can be a substitute for the GPS, using inertial sensors and a
374 Kalman observer to estimate the OCT position. However, the INS may result in large errors because of large
375 uncertainties associated with OCT drift, ocean currents, etc. Transponders on the seabed, in combination
376 with the INS, may increase the accuracy of the positioning system. However, large errors may persist.

377 Thus, in the following the OVC control system is designed assuming that position sensor measurements
378 are missing. Ten measurements are assumed available, i.e. deviations from nominal values of translational
379 and angular velocities, Euler angles, and rotor angular speed. The OVC control system is designed using
380 these measurements and $a = 5$, $W = 1.4\text{x}10^{-6}I$, $\lambda = 0.25$. For evaluation two scenarios are considered: 1) The
381 OCT is initially disturbed by 5 m laterally and 5 m vertically with respect to the nominal operating condition.
382 2) The OCT is persistently disturbed by white noise disturbances of the same intensities as the ones used in
383 OVC control design.

384 Fig. 17 shows a comparison between responses of the linear closed loop systems without position sensors
385 (solid lines) and with all sensors working (dotted lines) when these systems are subjected to an initial
386 perturbation in position (scenario 1). Figs. 18-19 show a comparison between the responses of the same
387 systems when they are subjected to white noise disturbances (scenario 2). It can be seen that elimination of
388 position sensor measurements has negligible effect on closed loop system performance. For example, in Fig.
389 18 the rotor blades experience very similar, small variations of the blade pitch angle control inputs, for both
390 closed loop systems. The maximum variation of the electromechanical torque is only about 18% of the trim
391 value. The rotor angular speed variation is also very small, with a maximum deviation of about 0.5 RPM.
392 Also note that negligible degradation of the closed loop system's response for the OCT Cartesian coordinates
393 is observed when position sensor measurements are missing. Similar remarks apply when responses to white
394 noise disturbances are compared. Fig. 19 shows that the OCT Euler angle variations around their nominal

values are small. The closed-loop system without position sensors achieves good performance because it uses information from rate gyros and translational velocity sensors to estimate OCT's position.

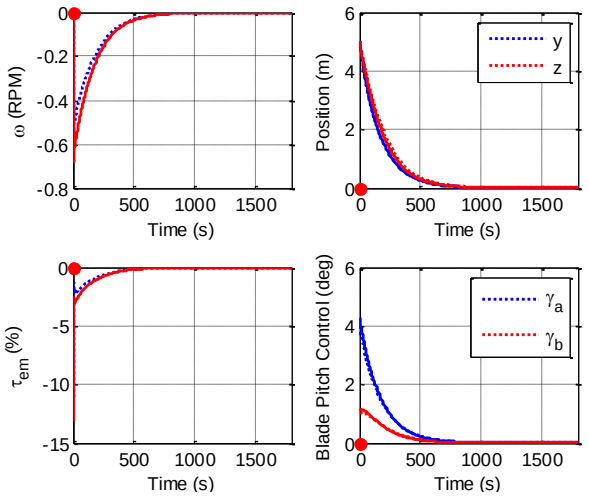

Fig. 17 System responses to initial condition perturbation (solid lines: without position sensors, dotted lines: with all sensors)

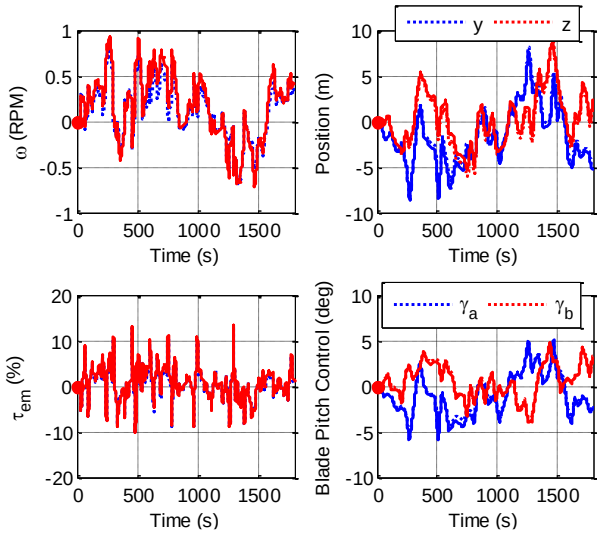

Fig. 18 System responses to white noise disturbances (solid lines: without position sensors, dotted lines: with all sensors)

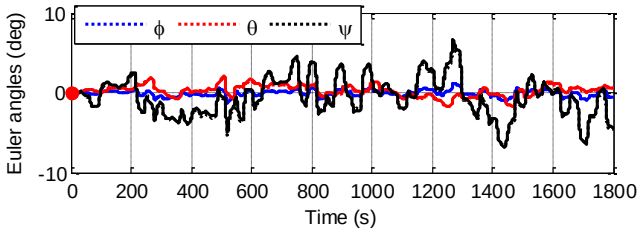

Fig. 19 Time histories of Euler angle deviations from nominal values (solid lines: without position sensors, dotted lines: with all sensors)

404 *G. OVC Control without Position and Velocity Sensors*

405 The OVC control system is also redesigned when position and translational velocity sensor measurements
406 are missing. For control design seven measurements (deviations from nominal values of angular velocities,
407 Euler angles, and rotor angular speed) and $a = 5$, $W = 1.4\text{x}10^{-6}I$, $\lambda = 0.25$, are used.

408 To illustrate the effect on the OVC control performance, Figs. 20-21 show responses of the linear closed
409 loop systems without position and translational velocity sensors (solid lines) and with all sensors working
410 (dotted lines) to white noise disturbances with the same intensities as those used in the OVC control design.
411 Fig. 20 shows that the maximum deviations of the OCT coordinates are significantly larger than those in the
412 nominal case: both *y* and *z* reach values of almost 9.5 m, whereas for the case with all sensors working their
413 maximum values are about 6.7 m. Also, the OVC controller employs 18% more torque and larger blade pitch
414 angle control inputs (almost up to 10°) when the system does not use position and translational velocity
415 measurements. Time histories of the Euler angle deviations from their nominal values suggest that these
416 states are not affected significantly by elimination of position and velocity measurements. This is expected
417 because Euler angles are available as measurements.

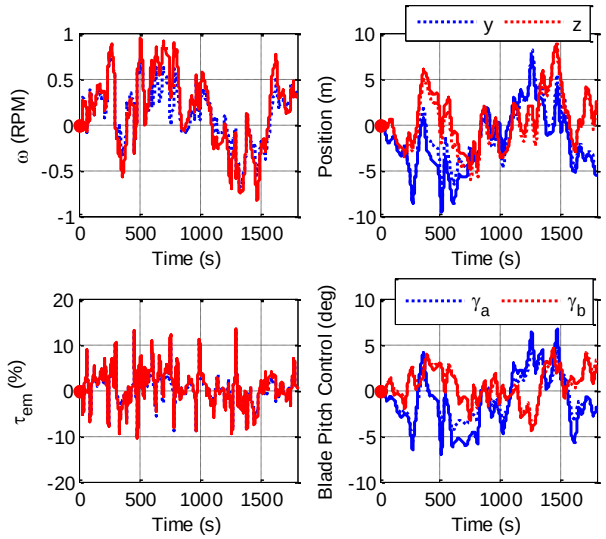

418

419 Fig. 20 System responses to white noise disturbances (solid lines: without position and velocity sensors, dotted lines: with all
420 sensors)

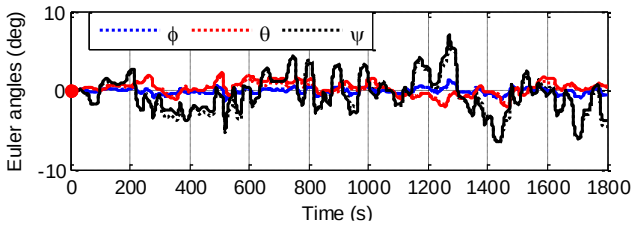

Fig. 21 Time histories of Euler angle deviations from nominal values (solid lines: without position sensors, dotted lines: with all sensors)

VI. Conclusions

A linearized model for a moored OCT was developed from a detailed nonlinear simulation model. Linear stability analysis revealed the existence of three very lightly damped modes. The corresponding slowly decaying open-loop behavior was found to primarily impact OCT position. This is detrimental to the safe and optimal operation of the OCT, which must operate in confined regions to avoid shipping traffic, yet close to the ocean surface to generate maximum power. Feedback control is therefore necessary to ensure sufficiently fast return to the nominal operating condition.

To improve OCT control system capabilities, a key control system technology innovation, inspired by helicopter technology, was introduced in the form of cyclic blade pitch angle control. This results in two control inputs, in addition to the standard electromagnetic torque applied to the rotor, which increase the authority of the OCT control system. OVC control designed with these three control inputs was found adequate to minimize control energy subject to variance constraints on deviations from the nominal values of lateral and vertical OCT inertial coordinates and rotor angular speed. Importantly, rapid return of the OCT to the unperturbed nominal operating condition was achieved using OVC control.

A parametric study with respect to the variance constraint limits revealed that control energy decreases rapidly when these limits depart from the minimum theoretically achievable bounds. This is important because practical OVC limits can be satisfied with relatively small control energy consumption. Also, small control energy corresponds to small control variations, which result in small blade pitch angles. This implies that effective control of OCT using OVC control systems with electromagnetic rotor torque and cyclic blade pitch angle control inputs can be achieved, avoiding the danger of blade stall.

Investigation into the effects of modeling errors, quantified by the process noise intensity, on the OVC control performance revealed that the likelihood of blade stall increases rapidly when process noise intensity increases. This observation emphasizes the need for accurate OCT control models. Another parametric study, for the influence of the control penalty matrix used in OVC control design, indicated that the blade pitch angle variations are relatively mild. By choosing a large control penalty matrix the danger of stall is alleviated.

Comparisons between linear and nonlinear simulations indicated that the current OCT linear model is sufficiently reliable for control design. Eventual discrepancies between nonlinear and linear closed loop responses were traced back to the cable dynamics which is taken into account in the nonlinear model but ignored in the linear model.

Our analysis indicated that when position sensor measurements are not available, the degradation in OVC control performance is negligible. It should be noted that this might be true in the short term, since we can estimate position from other measurements. However, maintaining position without direct position measurements for extended periods of time on an actual system is unlikely. Lastly, when both position and linear velocity sensor measurements are missing, this degradation may no longer be ignored.

VII. ACKNOWLEDGEMENT

This work was supported by NSF ECCS 1308168/1307827/1307889 and NSF ECCS 1809404/1809164/ 1809164.

VIII. APPENDIX

The nonlinear numerical simulation utilized in the paper was originally published in [13], with the associated algorithms summarized in this Appendix. Note that notations used next are inherent to this Appendix and should not be confused with notations used in the main body of the article. Likewise, equation numbering is intrinsic to this Appendix.

A. Kinematics

The five types of coordinate systems used in this analysis are the earth fixed coordinate system, $\Im_E$, the body fixed coordinate system, $\Im_B$, momentum mesh coordinate systems, $\Im_M^{ik}$, where $(\bullet)^i$ indicates the referenced blade element radial location on mesh azimuth angle grid point $(\bullet)^k$, the shaft coordinate system, $\Im_S$, and rotor blade coordinate systems, $\Im_R^{ij}$, where $(\bullet)^i$ indicates the referenced blade element on rotor blade $(\bullet)^j$. The origin of $\Im_E$ is located at mean sea level directly above the mooring connection assembly; with the X-axis pointing North, the Z-axis pointing downward, and the Y-axis pointing East to complete the right-hand rule. The origin of $\Im_B$ is fixed to the main body of the turbine and located at the center of the rotor shaft just behind the main pressure vessel; with the x-axis co-axial with the rotor shaft pointing from tail to nose, the z-axis points towards the bottom of the turbine, and the y-axis is aligned to complete the right-hand rule. The origin of each $\Im_M^{ij}$ is attached at the corresponding discrete mesh node that is fixed with respect to $\Im_B$ and utilize a polar co-ordinate system centered about the rotor shaft and covering the swept area of the rotor blade. For this coordinate system the axial direction, $(\bullet)_A^{ik}$, is parallel to the x-axis, the tangential direction, $(\bullet)_T^{ik}$, points in the rotor rotation direction, and the radial direction, $(\bullet)_R^{ik}$, points radially outward from the center of the rotor. The origin of the $\Im_S$ coordinate system is fixed to the shaft at the center of the hub and rotates with the rotor. This coordinate system has its x_s-axis co-axial with the x-axis, the z_s-axis perpendicular to the rotor shaft and parallel to rotor blade 1, and the y_s-axis is aligned to complete the right-hand rule. The origin of each $\Im_R^{ij}$ is fixed to the quarter cord line of each of the discrete rotor blade sections; with the axial direction, $(\bullet)_A^{ij}$, parallel to the x-axis, the tangential direction, $(\bullet)_T^{ij}$, in the rotor rotation direction, and the radial direction, $(\bullet)_R^{ij}$, pointing radially outward from the from the center of the rotor.

The relationship between $\Im_B$ and $\Im_E$ is defined using the Euler angles, which define the attitude of $\Im_B$ using three successive rotations about the yaw angle ψ, the pitch angle θ, and then the roll angle φ. The transformation matrix from $\Im_E$ to $\Im_B$ is defined as L_{EB}.

Calculations in each $\mathfrak{I}_M^{ik}$ consider the axial, radial, and tangential directions at a momentum mesh grid location that is fixed with respect to $\mathfrak{I}_B$. The constant transformation matrices from $\mathfrak{I}_B$ to $\mathfrak{I}_M^{ik}$ are defined by L_{BM}^k.

The transformation matrix from $\mathfrak{I}_B$ to $\mathfrak{I}_S$ is defined using the rotation angle δ of the rotor blade with respect to the turbine and denoted as L_{BS}.

The transformation matrices from $\mathfrak{I}_S$ to $\mathfrak{I}_R^{ij}$ are defined using the angle ς^j between the reference rotor blade (rotor blade 1) and the rotor blade of interest. Calculations in $\mathfrak{I}_R^{ij}$ consider the axial, radial, and tangential directions and this transformation matrix is denoted as L_{SR}^j. The utilized transformation matrices are all orthonormal and therefore the inverse of these transformation matrices is equal to their transpose.

B. Equations of motion

The equations of motion used in this simulation are derived from the 6-DOF rigid body equations of motion suggested by [31]. These six equations are first applied separately to both the rotor section and main body, with the forces and moments from the shaft applied to each system with the same magnitude but in opposite directions. These forces and moments are applied at the origin of $\mathfrak{I}_B$. As the motions of these systems are the same at the origin of $\mathfrak{I}_B$, except for the rotation about the x-axis, these 12 equations are reduced to 7 equations with 7 unknowns. These equations are then reduced to 7-DOF equations of motion by combining like terms and assuming symmetry for the main body about the xz-plane and symmetry of the inertial properties of the rotor about both the xz-plane and xy-plane. These equations of motion can be used to find the angular acceleration of the rotor directly using the system's states and inertial properties,

$$\dot{p}_r = [M_{x_r} - M_{x_s} - q\ r(I_{z_r}^v - I_{y_r}^v)]/I_{x_r}^v. \tag{A1}$$

The other six equations are coupled and therefore acceleration can be solved for by

$$\begin{bmatrix} \dot{u} \\ \dot{v} \\ \dot{w} \\ \dot{p}_b \\ \dot{q} \\ \dot{r} \end{bmatrix} = M^{-1}C \tag{A2}$$

where

$$M = \begin{bmatrix} m^v & 0 & 0 & 0 & m_b^v\ z_{G_b}^v & 0 \\ 0 & m^v & 0 & -m_b^v\ z_{G_b}^v & 0 & m^v\ x_G^v \\ 0 & 0 & m^v & 0 & -m^v\ x_G^v & 0 \\ 0 & -m_b^v\ z_{G_b}^v & 0 & I_{x_b}^v & 0 & -I_{xz_b}^v \\ m_b^v\ z_{G_b}^v & 0 & -m^v\ x_G^v & 0 & I_y^v & 0 \\ 0 & m^v\ x_G^v & 0 & -I_{xz_b}^v & 0 & I_z^v \end{bmatrix}$$

$$C = \begin{bmatrix} f_x + m^v(v\ r - w\ q) + m^v\ x_G^v(q^2 + r^2) - m_b^v\ z_{G_b}^v\ p_b\ r \\ f_y - m^v\ u\ r + w(m_b^v\ p_b + m_r^v\ p_r) - m_b^v\ z_{G_b}^v\ q\ r - m_b^v\ x_{G_b}^v\ q\ p_b - m_r^v\ x_{G_r}^v\ q\ p_r \\ f_z + m^v\ u\ q - v(m_b^v\ p_b + m_r^v\ p_r) + m_b^v\ z_{G_b}^v(p_b^2 + q^2) - m_b^v\ x_{G_b}^v\ r\ p_b - m_r^v\ x_{G_r}^v\ r\ p_r \\ M_{x_b} + M_{x_s} - q\ r(I_{z_b}^v - I_{y_b}^v) + I_{xz_b}^v\ p_b\ q - m_b^v\ z_{G_b}^v(wp_b - u\ r) \\ M_y - r\ p_b(I_{x_b}^v - I_{z_b}^v) - r\ p_r(I_{x_r}^v - I_{z_r}^v) - I_{xz_b}^v(p_b^2 - r^2) + m_b^v\ z_{G_b}^v(v\ r - w\ q) - m^v\ x_G^v\ u\ q + m_b^v\ x_{G_b}^v\ v\ p_b + m_r^v\ x_{G_r}^v\ v\ p_r \\ M_z - q\ p_b(I_{y_b}^v - I_{x_b}^v) - q\ p_r(I_{y_r}^v - I_{x_r}^v) - I_{xz_b}^v\ r\ q - m^v\ x_G^v\ u\ r + m_b^v\ x_{G_b}^v\ w\ p_b + m_r^v\ x_{G_r}^v\ w\ p_r \end{bmatrix}$$

The symbol $(\dot{\bullet})$ denotes the time derivative; $(\bullet)^v$ denotes that the virtual mass, virtual mass moment of inertia, virtual product of inertia, or virtual center of gravity; $(\bullet)_r$ denotes the rotor portion of the system (everything attached to the rotor and aft of the shaft); $(\bullet)_b$ denotes the main body portion of the system (everything that is not attached to the rotor and aft of the shaft); $(\bullet)_G$ denotes the center of gravity; M_{x_s} denotes the shaft moment about the x-axis that the shaft induces on the main body; m is the mass of the entire OCT or the component denoted by a subscript; $p_{\bullet}$ denotes the rotational velocities about the x-axis with the subscript denoting a reference to either the main body or the rotor; q and r are the rotational velocities common to both the rotor and main body about y and z respectively; u, v, and w are the linear velocities in the x, y, and z directions; $f_{\bullet}$ denotes the total external force in the direction of its subscript; $M_{\bullet}$ denotes the total external moment about the axis denoted by its subscript; $I_{\bullet}$ denotes the mass moment or product of inertia denoted by its subscript, and $[\bullet]^{-1}$ denotes the inverse operator. The virtual masses, moments of inertia, and products of inertia are estimated as being twice the actual masses, moments of

528 inertia, and products of inertia of the OCT and the virtual center of mass is assumed to be at the same location
529 as the actual center of mass.

530 *C. Hydrostatics*

531 This mathematical model assumes that the turbine is completely submerged, with constant gravitational
532 and buoyancy force magnitudes. Using the individual masses and buoyancies of each component, scaled
533 from a paper design of an experimental ocean current turbine [21]; the total mass, m, total buoyancy, B,
534 center of mass (gravity), CG, and center of buoyancy, CB, are calculated. These values are used to calculate
535 the combined gravitational and buoyancy forces of the entire system in $\mathfrak{I}_B$, and the hydrostatic moments
536 about the origin of $\mathfrak{I}_B$:

537 $$f_{GB} = L_{EB}^{(3,:)}(m\ g - B) \text{ and} \tag{A3}$$

538 $$M_{GB} = -B(CB - CG) \times L_{EB}^{(3,:)}, \tag{A4}$$

539 respectively, where $(\times)$ denotes the cross product, $(\bullet)^{(3,:)}$ denotes a reference to a vector consisting of all
540 elements in the third column of the referenced matrix, and g is the gravitational constant.

541 *D. Rotor Force Modeling*

542 The mathematical rotor model uses an unsteady form of the Blade Element Momentum (BEM) approach
543 to calculate the forces on the rotor blades.

544 *1) Lift and Drag Coefficients*

545 The 2D lift and drag coefficients for hydrofoils described in [14] are found using Xfoil [32]. The program
546 AirfoilPrep [33] is then used to convert these coefficients to their 3D rotor blade equivalent by first
547 considering the 3D stall characteristics and then extrapolating the lift and drag coefficient over all possible
548 angles of attack. This calculation of 3D rotor blade coefficients uses Selig Du correction [34] and Eggars
549 coefficient of drag adjustment [35], which considers the radial location of the airfoil sections and the aspect
550 ratio. To extrapolate these 3D coefficients beyond stall, the Viterna method [36] is used as presented by [37],
551 which calculates the coefficients of lift and drag for deep stall. Using the 3D lift and drag coefficients, the

552 lift, $C_L^{ij}(\alpha^{ij})$, and drag, $C_D^{ij}(\alpha^{ij})$, coefficients for each hydro foil section is calculated as a function of angle
553 of attack, α^{ij}, by interpolating the data from the airfoil shapes based on the radial location of each section.

554 *2) Unsteady Blade Element Momentum Rotor Model*
555 The hydrodynamic forces on the rotor are calculated using an unsteady BEM rotor model similar to the
556 one presented in [23]. This approach uses the 3D lift and drag coefficients, which are a function of angle of
557 attack. The effect of the rotor on the incoming flow is calculated with respect to $\Im_M^{ik}$. This mesh has nodes at
558 distances from the hub that are equivalent to the radial locations of the center of blade elements and therefore
559 are denoted by $(\bullet)^i$. This mesh is also divided into M_δ angular sections spaced evenly with respect to the
560 azimuth angle, with the angle component of the matrix denoted by $(\bullet)^k$. The impeded flow at each rotor
561 blade element is calculated using the momentum model with values interpolated from the adjacent radial
562 grid points. Conversely, the wake induced water velocity at the mesh grid points, used by the momentum
563 model, are calculated as if a blade element were at each grid point. Since individual blade pitch is allowed,
564 the blade pitch angle of the most recent blade to pass each location, at its time of passage, is used. Therefore,
565 both the actual rotor forces and the rotor forces used for the momentum model are calculated each time step.
566 Angle of attack is calculated for each discrete section $(\bullet)^i$ of both rotor blade $(\bullet)^j$ and mesh grid azimuth
567 angle $(\bullet)^k$ as a function of the axial, $\bar{V}_A^{ij,ik}$, and tangential, $\bar{V}_T^{ij,ik}$, components of relative water velocity by:

568 $$\bar{V}^{ij,ik} = V_o^{ij,ik} + V_{blade}^{ij,ik} + W^{ij,ik}(n-1), \tag{A5}$$

569 where $V_o^{ij,ik}$ is the undisturbed free stream water velocity, $V_{blade}^{ij,ik}$ is the effect of the motions of the blade
570 elements or related mesh points on the relative water velocity, and $W^{ij,ik}(n-1)$ is the wake induced water
571 velocity from the previous time step at the location of the mesh grid and respective blade elements. Note:
572 $V_{blade}^{ij,ik}$ is calculated from

573 $$V_{blade}^{ij} = -L_{SR}^{j} L_{BS} \left[\begin{bmatrix} u \\ v \\ w \end{bmatrix} + \begin{bmatrix} p_r \\ q \\ r \end{bmatrix} \times \begin{bmatrix} x^{ij} \\ y^{ij} \\ z^{ij} \end{bmatrix} \right] \text{ and} \tag{A6}$$

$$V_{blade}^{ik} = -L_{BM}^{k}\left[\begin{bmatrix} u \\ v \\ w \end{bmatrix} + \begin{bmatrix} p_r \\ q \\ r \end{bmatrix} \times \begin{bmatrix} x^{ik} \\ y^{ik} \\ z^{ik} \end{bmatrix}\right], \quad \text{(A7)}$$

$V_o^{ij,ik}$ is calculated from

$$V_o^{ij} = L_{SR}^{j} L_{BS} L_{EB} \begin{bmatrix} U_w^{ij} \\ V_w^{ij} \\ W_w^{ij} \end{bmatrix} \text{ and} \quad \text{(A8)}$$

$$V_o^{ik} = L_{BM}^{k} L_{EB} \begin{bmatrix} U_w^{ik} \\ V_w^{ik} \\ W_w^{ik} \end{bmatrix}, \quad \text{(A9)}$$

where the undisturbed water velocities in $\Im_E$ are functions of the wave field, current profile, blade element or mesh grid location, and time.

The angle of attack of each element section is calculated by

$$\alpha^{ij,ik} = \phi^{ij,ik} - \beta^{ij,ik}, \quad \text{(A10)}$$

where the relative flow angle is calculated by

$$\phi^{ij,ik} = tan^{-1}\left(\frac{\bar{V}_A^{ij,ik}}{-\bar{V}_T^{ij,ik}}\right) \quad \text{(A11)}$$

and $\beta^{ij,ik}$ is the blade section pitch angle.

The lift coefficient matrix, $C_L^{ik}(\alpha^{ik})$, calculated over the mesh field for the angles of attack calculated using (A10) is used to calculate the lift per unit length, L^{ik}, that is used in (A17) and (A18) for calculating the quasi-static wake field. Additionally, both the lift and drag coefficient matrices, $C_L^{ij}(\alpha^{ij})$ and $C_D^{ij}(\alpha^{ij})$, found using the angles of attack calculated in (A10) are used to calculate the axial (normal), C_A^{ij}, and tangential, C_T^{ij}, force coefficients respectively [23].

These coefficients are then used to estimate the axial and tangential loads on each of the blade sections by

$$f_A^{ij} = \frac{1}{2}\ \rho\ \delta r^i\ c^i\ C_A^{ij}((\bar{V}_A^{ij})^2 + (\bar{V}_T^{ij})^2) \text{ and} \quad \text{(A12)}$$

$$f_T^{ij} = \frac{1}{2}\ \rho\ \delta r^i\ c^i\ C_T^{ij}((\bar{V}_A^{ij})^2 + (\bar{V}_T^{ij})^2), \tag{A13}$$

where ρ is the density of seawater, δr^i is the radial length of element $(\bullet)^i$, and c^i is the cord length at the center of section $(\bullet)^i$. These forces are converted to $\Im_B$ by using the appropriate transformation matrices. Using the forces on the discrete sections of the rotor, the total force on the rotor is found. Similarly, the hydrodynamic moment from the rotor about the origin of $\Im_B$ (the rotor axis) is calculated using the forces calculated on the individual blade components and their relative locations.

The second part of applying the unsteady BEM rotor model is calculating the effect of the rotor on the flow field. As mentioned previously, the effect of the rotor on the incoming flow is calculated over a mesh of points spread over the swept area of the rotor blade using a polar coordinate system that is fixed with respect to $\Im_B$. To account for the end effects of the rotor blade on the flow field, Prandtl's tip loss correlation factor is first calculated as suggested by [23]:

$$F^{ik} = \frac{2}{\pi} cos^{-1}\left(e^{-\frac{B(R-r^i)}{2\ r^i\ sin\,\phi^{ik}}}\right), \tag{A14}$$

where B is the number of blades and R is the rotor radius.

The axial induction factor calculated using the wake field from the previous time step is defined by [23] as

$$a^{ik} = \frac{W_A^{ik}(n-1)}{\|\boldsymbol{V}_o^{ik}\|_2}, \tag{A15}$$

where $\|\bullet\|_2$ denotes the l_2 or Euclidean norm. Using this axial induction factor, the Glauert correction is calculated by

$$f_g^{ik} = \begin{cases} 1 & for\ a^{ik} \le a_c, \\ \frac{a_c}{a^{ik}}(2 - \frac{a_c}{a^{ik}}) & for\ a^{ik} > a_c \end{cases} \tag{A16}$$

where $a_c = 0.2$ as suggested by [23]. The quasi-static wake field is now calculated in terms of its axial and tangential components for time step n [23]:

$$W_{A_{qs}}^{ik}(n) = \frac{-B\ L^{ik}\ cos(\phi^{ik})}{4\ \pi\ \rho\ r^{i}\ F^{ik}\sqrt{(V_A^{ik}+f_g^{ik}\ W_{A_o}^{ik}(n-1))^2+(V_R^{ik})^2+(V_T^{ik})^2}} \text{ and} \quad \text{(A17)}$$

$$W_{T_{qs}}^{ik}(n) = \frac{-B\ L^{ik}\ sin(\phi^{ik})}{4\ \pi\ \rho\ r^{i}\ F^{ik}\sqrt{(V_A^{ik}+f_g^{ik}\ W_{A_o}^{ik}(n-1))^2+(V_R^{ik})^2+(V_T^{ik})^2}}, \quad \text{(A18)}$$

where $(\bullet)_o$ denotes that the utilized wake field is not corrected for the wake skew angle (A21) and L^{ik} is the lift per unit length. To account for the time delay before the axial and tangential wake fields reach their equilibrium values, a dynamic wake model is used [23]. Following the method suggested by S. Oye, a filter is used that consists of two first order differential equations [23]. These differential equations can be solved analytically using the intermediate wake variable vectors, H^{ik} and W_{int}^{ik}, as follows [23]:

$$H^{ik} = W_{qs}^{ik}(n) + k\tau_1 \frac{W_{qs}^{ik}(n)-W_{qs}^{ik}(n-1)}{\Delta t}, \quad \text{(A19)}$$

$$W_{int}^{ik}(n) = H^{ik} + \left(W_{int}^{ik}(n-1) - H^{ik}\right)e^{-\Delta t/\tau_1}, \text{ and} \quad \text{(A20)}$$

$$W_{o}^{ik}(n) = W_{int}^{ik}(n) + \left(W_{o}^{ik}(n-1) - W_{int}^{ik}(n)\right)e^{-\Delta t/\tau_2}. \quad \text{(A21)}$$

For these equations the time constants τ_1 and τ_2 are calculate as suggested by [23]:

$$\tau_1 = \frac{1.1}{(1-1.3a_1^{ik})}\frac{R}{V_o} \text{ and} \quad \text{(A22)}$$

$$\tau_2 = (0.39 - 0.26\left(\frac{r^j}{R}\right)^2)\tau_1, \text{ where} \quad \text{(A23)}$$

$$a_1^{ik} = \begin{cases} a^{ik} & for\ a^{ik} < 0.5 \\ 0.5 & for\ a^{ik} > 0.5 \end{cases}. \quad \text{(A24)}$$

The wake model used in this numerical simulation has been calculated for discrete locations over the swept area of the rotor blade with the mesh fixed with respect to $\Im_B$. To estimate the wake at the blade elements, $W_o^{ij}(n)$, the wake is linearly interpolated between the closest two azimuth angles in mesh grid $W_o^{ij}(n)$ for the same radial location:

$$W_o^{ij}(n) = f(W_o^{ik}(n), \delta_m^k). \quad \text{(A24)}$$

A yaw model is included in this simulation so that the unsteady BEM method will predict the restoring yaw moment [23]. The method proposed by Glauert is used to calculate the wake field corrected for yaw [23] by

$$W^{ij,ik}(n) = W_o^{ij,ik}(n)(1 + \frac{r^i}{R} tan(\frac{\chi}{2}) cos(\theta_{wing} - \theta_o)), \quad \text{(A25)}$$

where the wake skew angle, χ, is defined as the angle between the current velocity in the wake and the rotational axis of the rotor and θ_o is the angle where the blade is deepest into the wake. The skew angle can be found by

$$\chi = tan\,2^{-1}\left(\left\|\sum_{k=1}^{M_\delta}(\widetilde{W}_y^k + \tilde{V}_y^k), \sum_{k=1}^{M_\delta}(\widetilde{W}_z^k + \tilde{V}_z^k)\right\|_2, -\sum_{k=1}^{M_\delta}(\widetilde{W}_x^k + \tilde{V}_x^k)\right), \quad \text{(A26)}$$

where $tan\,2^{-1}$ (•,•) denotes the four-quadrant inverse tangent function and ($\tilde{\bullet}$) denotes that the skew angle is assumed to be constant with radius and is calculated at $r^i/R = 0.7$ as suggested by [23].

E. Streamline body force modeling

The main turbine body that houses the generator and the two buoyancy compensation modules are somewhat streamlined bodies. To calculate the drag forces on these components constant drag coefficients are used. For the axial drag on the buoyancy compensation modules, $Cd_x^{SL} = 0.2$, and for the main turbine body, $Cd_x^{SL} = 0.4$. A constant coefficient is also used for the tangential drag on across all three of these bodies, $Cd_\perp^{SL} = 1.0$. The drag forces and resulting moments on these bodies are calculated using the mean axial relative velocity to calculate the axial forces and by numerically integrated the relative velocity to calculate off axis forces.

F. Cable Force Model

A finite element lumped mass cable model is used for the cable that attaches the turbine to the flounder plate. Each element is modeled as being linear, with the position and velocity of the end nodes defined by the orientation and velocity of the turbine and the position of the flounder plate. The force on each cable node can be found using a method presented by [38 and 39]. This cable model includes forces from gravity, buoyancy, hydrodynamic drag, and internal strain.

G. Environmental Models

The environmental disturbances included in this simulation are calculated using both current and wave models. These current and wave models are used to calculate the undisturbed free stream water velocity utilized by the rotor model in (A10), and when calculating the relative free stream water velocities utilized to calculate the forces on the streamline bodies. The undisturbed free stream water velocity is calculated from:

$$V_W^{ij,ik} = V_{W_C}^{ij,ik} + V_{W_W}^{ij,ik}, \tag{A27}$$

where $V_W^{ij,ik}$ is the free stream water velocity in $\Im_E$, $V_{W_C}^{ij,ik}$ is the current induced free stream water velocity in $\Im_E$, and $V_{W_W}^{ij,ik}$ is the wave induced free stream water velocity in $\Im_E$ (A28).

1) Current model

The ocean current induced free stream water velocity is modeled as varying linearly with depth. The water velocity vector at the surface and the vertical gradient of the current are used to calculate the free stream water velocity each time step for based on the instantaneous depth of each turbine component.

2) Wave model

A wave model is included in the simulation to estimate the impact of a wave field on the performance of an OCT. This model is presented in detail by [26] and is summarized here for the reader's convenience. The orbital water velocity induced by the wave field is calculated each time step for each location on the OCT where the hydrodynamic force is calculated.

This simulation assumes a fully developed sea using a wave spectrum which is the product of a frequency spectrum and a directional spreading function. A Pierson-Moskowitz spectrum is used to model the frequency spectrum portion, $S(\omega_i)$, of this wave model [40]. The propagation direction of the individual wave components is calculated using a cosine "2s" directional spreading function, $D(\Theta_i)$, based on the work of Pierson in 1955 [41]. A spreading value of 10 is recommended for wind waves, 25 for swell with short decay and 75 for swell with long decay distance [42]. The orbital velocities from the individual wave

components calculated from this spectrum are assumed to decay with depth according to linear wave theory [43]. The orbital water velocities are calculated for each of the N_W wave components, $(\bullet)^i$, according to:

$$V_{WW}^{ij,ik} = \begin{bmatrix} \sum_{i=1}^{N_W} \left[\frac{H_i\ g\ k_i}{2\ \omega_i} \frac{cosh\left(k_i(h-Z^{ij,ik})\right)}{cosh(k_i\ h)} cos\left(k_i\ p_i^{ij,ik} - \omega_i\ t + \varphi_i\right) cos(\Theta_i + \Theta_0) \right] \\ \sum_{i=1}^{N_W} \left[\frac{H_i\ g\ k_i}{2\ \omega_i} \frac{cosh\left(k_i(h-Z^{ij,ik})\right)}{cosh(k_i\ h)} cos\left(k_i\ p_i^{ij,ik} - \omega_i\ t + \varphi_i\right) sin(\Theta_i + \Theta_0) \right] \\ \sum_{i=1}^{N_W} \left[\frac{-H_i\ g\ k_i}{2\ \omega_i} \frac{sinh\left(k_i(h-Z^{ij,ik})\right)}{cosh(k_i\ h)} sin\left(k_i\ p_i^{ij,ik} - \omega_i\ t + \varphi_i\right) \right] \end{bmatrix}, \text{ with (A28)}$$

$$H_i = \sqrt{2\ S(\omega_i)\ D(\Theta_i)\ \Delta\omega\ \Delta\Theta} \text{ and}$$

$$p_i^{ij,ik} = X^{ij,ik}\ cos(\Theta_i + \Theta_0) + Y^{ij,ik}\ sin(\Theta_i + \Theta_0),$$

where H_i is the wave component amplitude, ω_i is the wave component frequency, k_i is the wave component number, Θ_i is the wave component direction with respect to the mean wave propagation direction Θ_0, φ_i is the random phase angle which is uniformly distributed from 0 to 2π and constant with time, h is the water depth, t is the time in seconds, $\Delta\omega$ is the frequency step sized used discretizing the frequency spectra, and $\Delta\Theta$ is the angular step size used when discretizing the spreading function.

Linear wave theory for deep water waves predicts the orbital velocity at the surface for each wave component, and that this orbital water velocity will decay with depth according to $exp(-4\ \pi^2\ Z/(g\ T_c^2))$. Applying these relationships to a single wave component with $H_c = 1.859$ m and $T_c = 6.8$ s, both the horizontal and vertical water velocity magnitudes will be 0.86 m/s at the surface and these velocities will decay according to $exp(-0.087 \cdot Z)$. This shows that at a depth of 8.0 m the wave induced water velocities will be 50% of those at the surface and that at depth of 30 m the water velocities decreased to only 7% of the surface velocity.

IX. References

[1] K. Hass, "Assessment of energy production potential from ocean currents along the United States coastline," Georgia Tech Research Corp., Atlanta, GA, Tech. Rep. DOE/EE/2661-10, 2013.

[2] M. C. P. M. Machado, J. H. VanZwieten, I. Pinos, "A measurement based analysis of the hydrokinetic energy in the Gulf stream," *Journal of Ocean and Wind Energy*, vol. 3, pp. 25-30, 2016.

[3] J. T. Imamura, K. Takagi, T. Waseda, and K. Kiyomatsu, "Kuchinoshima island ocean current measurements for Kuroshio current energy," in *Proc. IEEE/MTS Oceans Conference*, Monterey, CA, USA, Sep. 19-23, 2016.

[4] I. Meyer, J. L. Van Niekerk, "Towards a practical resource assessment of the extractable energy in the Agulhas ocean current," *International Journal of Marine Energy*, vol. 16, pp. 116-132, Dec. 2016.

[5] J. M. Bane, R. He, M. Muglia, C. F. Lowcher, Y. Gong, and S. M. Haines, "Marine hydrokinetic energy from western boundary currents," *Annu. Rev. Mar. Sci.*, vol. 9, pp. 105–23, 2017.

[6] N. Tom and R. W. Yeung, "Experimental confirmation of nonlinear-model- predictive control applied offline to a permanent magnet linear generator for ocean-wave energy conversion," *IEEE Journal of Oceanic Engineering*, vol. 41, no. 2, pp. 281-295, Apr. 2016.

[7] W. Sheng and A. Lewis, "Power takeoff optimization for maximizing energy conversion of wave-activated bodies", *IEEE Journal of Oceanic Engineering*, vol. 41, no. 3, pp. 529-540, Jul. 2016.

[8] W. Sheng and A. Lewis, "Power takeoff optimization to maximize wave energy conversions for oscillating water column devices," *IEEE Journal of Oceanic Engineering*, vol. 43, no. 1, pp. 36-46, Jan. 2018.

[9] H. T. Pham, J. M. Bourgeot, and M. E. H Benbouzid, "Comparative investigations of sensor fault-tolerant control strategies performance for marine current turbine applications," IEEE Journal of Oceanic Engineering, vol. 43, no. 4, pp. 1024-1035, Oct. 2018.

[10] J. H. VanZwieten, F. R. Driscoll, A. Leonessa, and G. Deane, "Design of a prototype ocean current turbine—part ii: flight control system," *Ocean Eng.*, vol. 33, pp. 1522–1551, Aug. 2006.

[11] K. Takagi, Y. Suyama, K. Kagaya, "An attempt to control the motion of floating current turbine by the pitch control," in *Proc. IEEE/MTS Oceans Conference*, Waikoloa, HI, USA, Sep. 19-22, 2011.

[12] K. Sakata, T. Gonoji, K. Takagi, "A motion of twin type ocean current turbines in realistic situations," in *Proc. IEEE/MTS Oceans Conference*, Yeosu, South Korea, May 21-24, 2012.

[13] J. H. VanZwieten, N. Vanrietvelde, and B. L. Hacker, "Numerical simulation of an experimental ocean current turbine," *IEEE Journal of Oceanic Engineering*, vol. 38, no. 1, Jan. 2013.

[14] J. H. VanZwieten, P. Pyakurel, T. Ngo, C. Sultan, and N.I. Xiros, "An assessment of using variable blade pitch for moored ocean current turbine flight control," *International Journal of Marine Energy*, vol. 13, pp. 16-26, Apr. 2016.

[15] R. E. Skelton, and M. D. Lorenzo, "Space structure control design by variance assignment," *Journal of Guidance, Control, and Dynamics*, vol. 8, no. 4, pp. 454-462, Jul. 1985.

[16] R. E. Skelton, and C. Sultan, "Controllable tensegrity, a new class of smart structures," in *Proc. SPIE Intl. Symposium on Smart Structures and Materials*, San Diego, CA, USA, 1997.

[17] C. Sultan, and R. E. Skelton, **"**Integrated design of controllable tensegrity structures," in *Proc. ASME Intl. Mechanical Engineering Congress and Exposition*, Dallas, TX, 1997.

[18] T. Oktay, and C. Sultan, "Comfortable helicopter flight via passive/active morphing," *IEEE Transactions on Aerospace and Electronic Systems*, vol. 51, no. 4, Oct. 2016.

[19] G. Zhu, K. M. Grigoriadis, and R. E. Skelton, "Covariance control design for Hubble space telescope," *Journal of Guidance, Control, and Dynamics*, vol. 18, no. 2, pp. 230-236, Mar. 1995.

[20] T. D. Ngo, C. Sultan, J. H. VanZwieten, and N.I. Xiros, "Variance constrained cyclic blade control of moored ocean current turbines," in *Proc. American Control Conference*, Boston, MA, USA, 2016.

[21] F. R. Driscoll, G. M. Alsenas, P. P. Beaujean, S. Ravenna, J. Raveling, E. Busold, and C. Slezycki, "A 20 KW open ocean current test turbine," in *Proc. MTS/IEEE Oceans Conference*, Quebec City, Canada, Sep. 15-18, 2008.

[22] National Renewable Energy Laboratory, "Certification of FAST and ADAMS® with AeroDyn". Available: https://nwtc.nrel.gov/SimulatorCertification

[23] M. O. L. Hansen, *Aerodynamics of Wind Turbines*. London, UK: Earthscan, 2008.

[24] F.R. Driscoll, R.G. Lueck, and M. Nahon, "Development and validation of a lumped-mass dynamics model of a deep-sea ROV system," *Applied Ocean Research*, vol. 22, no. 3, pp. 169–182, Jun. 2000.

[25] B. Radanovic, and F.R. Driscoll, "Development of an efficient general purpose cable model and simulation for marine applications," in *Proc. IEEE Oceans Conference*, Biloxi, MI, USA, Oct. 29-31, 2002.

[26] N. Vanrietvelde, "Numerical performance prediction for FAU's first generation ocean current turbine," M.S. thesis, Dept. Ocean and Mech. Eng., Florida Atlantic University, 2009.

[27] G. D., Padfield, *Helicopter Flight Dynamics* (AIAA Education Series), 2nd ed. Reston, VA, USA: AIAA, 2007.

[28] N.I. Xiros, J.H. VanZwieten, C. Sultan, and V. Tzelepis, "Modeling, system identification and linearization of underwater turbine power plant dynamics," in *Proc. ASME International Mechanical Engineering Congress & Exposition*, Houston, TX, USA, no. IMECE2015-53455, November 13-19, 2015.

[29] G. Zhu, M. A. Rotea, and R. Skelton, "A convergent algorithm for the output covariance constraint control problem," *SIAM Journal of Control Optimization*, vol. 35, no. 1, pp. 341-361, Jan. 1997.

[30] C. Hsieh, R. Skelton, and F. M. Damra, "Minimum energy controllers with inequality constraints on output variances," *Optimal Control Applications and Methods*, vol. 10, no. 4, pp. 347-366, Oct. 1989.

[31] T. I. Fossen, *Guidance and control of ocean vehicles*. New York: John Wiley and Sons, 1994, pp. 10,30.

[32] M. Drela "XFoil: An analysis and design system for low Reynolds number airfoils," in *Proc. Conf. on low Reynolds Number Airfoil Dynamics*, University of Notre Dame, 1989

[33] C. Hansen, "AirfoilPrep - NWTC design codes," National Wind Technology Center – National Renewable Energy Laboratory, Golden, CO, 2007,

[34] Z. Du and M. S. Selig "A 3-D stall-delay model for horizontal axis wind turbine performance prediction," In *Proc. ASME Wind Energy Symp.*, Reno, NV, Jan. 12-15 1998, A98-16844 03-44

[35] A. Eggers, K. Chaney, and R. Digumarthi, "An assessment of approximate modeling of aerodynamic loads on the UAE rotor," In *Proc. 41st Aerospace Sciences Meeting and Exhibit*, Reno, NV, Jan. 6-9 2003, AIAA-2003-868

[36] L. A. Viterna and DC Janetzke "Theoretical and experimental power from large horizontal-axis wind turbines" *Pres. 5th Biennial Conf. and Workshop on Wind Energy*, Washington D.C., Oct. 5-7 1981,

[37] D. J. Laino and A. C. Hansen "User's guide to the wind turbine aerodynamics computer software AeroDyne," National Wind Technology Center – National Renewable Energy Laboratory, Golden, CO, Dec. 2002.

[38] B. Radanovic, "Development of an efficient general purpose cable model and simulation for marine applications," M.S. thesis, Dept. Ocean Eng., Florida Atlantic Univ., Boca Raton, FL, 2002.

[39] J. VanZwieten, F. R. Driscoll, A. Leonessa, and G Deane, "Design of a prototype ocean current turbine – Part I: mathematical modeling and dynamics simulation," *Ocean Eng.*, vol 33, pp. 1485-1521, Aug. 2006,

[40] W. J. Pierson, and L. Moskowitz, 1963 "A proposed spectral form for fully developed wind seas based on the similarity theory of S. A. Kitaigorodsku," *J. Geophysical Research*, vol. 69, no. 24, pp. 5181-5190, 1964,

[41] M. S. Longuet-Higgins, D. E. Cartwright, and N. D. Smith, “Observations of the directional spectrum of sea waves using the motion of a floating buoy,” in *Proc. Conf. Ocean Wave Spectra*”, 1963, pp.111-136

[42] Y. Goda, *Random seas and design of maritime structures*. Tokyo, Japan: University of Tokyo press, 1985, ch. 2

[43] R. G. Dean and R. A. Dalrymple, *Water wave mechanics for engineers and scientists*. River Edge, NJ: World Scientific, 1991, pp. 86